

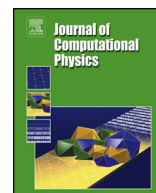


ELSEVIER

Contents lists available at ScienceDirect

Journal of Computational Physics

www.elsevier.com/locate/jcp



Low Mach number algorithm for droplet-laden turbulent channel flow including phase transition

A. Bukhvostova ^{a,*}, J.G.M. Kuerten ^{a,b}, B.J. Geurts ^{a,c}

^a Multiscale Modeling and Simulation, University of Twente, Faculty EEMCS, PO Box 217, 7500 AE Enschede, The Netherlands

^b Eindhoven University of Technology, Department of Mechanical Engineering, PO Box 513, 5600 MB Eindhoven, The Netherlands

^c Fluid Mechanics Laboratory, Eindhoven University of Technology, Department of Technical Physics, PO Box 513, 5600 MB Eindhoven, The Netherlands

ARTICLE INFO

Article history:

Received 19 May 2014

Received in revised form 6 March 2015

Accepted 15 April 2015

Available online 23 April 2015

Keywords:

Compressible flow

Low Mach number algorithm

Two-phase flow

Droplet-laden turbulent channel flow

ABSTRACT

In this study we propose a new numerical algorithm for droplet-laden turbulent channel flow with phase transitions at low Mach numbers. The carrier gas is treated as compressible flow. In order to avoid very small time steps at low Mach numbers that would arise from stability requirements associated with explicit time-stepping we propose a new semi-explicit time integration method, applied to the low Mach number compressible flow equations. We perform a perturbation analysis in powers of the Mach number of the system of governing equations. The obtained decomposition of pressure into a space-independent part and a hydrodynamic part permits to apply a special pressure-based time integration algorithm for compressible flows at low Mach numbers. An important feature of the new numerical approach is the independence of the maximum allowed time step on the Mach number. In this study we validate the new method by comparing it with a fully explicit code for compressible flow at general Mach numbers showing a good agreement in all quantities of interest. The differences between the results of the two codes are on the order of the square of the Mach number caused by the disregard of high-order terms in the Mach number in the new algorithm. The relative difference found for a specific low value of the Mach number of 0.05 is on the order of 1% for instantaneous and mean quantities of the two phases. We also quantify the efficiency of the new algorithm by comparing the computational time it takes to simulate one time unit with both codes.

© 2015 Elsevier Inc. All rights reserved.

1. Introduction

Multiphase flows with a large number of droplets dispersed into a gas play an important role in a variety of technological applications and environmental problems. Examples include thermal processing in food manufacturing, air pollution control and heat transfer in power stations [1]. In this paper we investigate a coupled Euler–Lagrange model to simulate droplet-laden turbulent channel flow in which phase transition plays an important role. The first such Euler–Lagrange study of mass and heat transfer in droplet-laden turbulent flow was done by Mashayek in 1998 [2]. He conducted a simulation study, investigating homogeneous turbulence with two-way coupling between the gas and the dispersed droplet phase involving momentum, mass and energy of the system. Later, a study dedicated to the mixing layer with embedded evaporating

* Corresponding author. Tel.: +31 53 489 3383.

E-mail address: a.bukhvostova@utwente.nl (A. Bukhvostova).

droplets was conducted by Miller and Bellan [3]. In [4] a cloud of inertial evaporating droplets, interacting with a non-isothermal droplet-laden turbulent planar jet, is considered. In the present paper we present a new time-stepping algorithm tailored to compressible flow at low Mach numbers and extend the work of Mashayek [2] to wall-bounded turbulence by investigating turbulent channel flow with a dispersed droplet phase undergoing phase transition. The models adopted here are identical to the models used in [3] and [4]. The main difference between the current study and the studies mentioned above is that we consider conditions in which not only evaporation of droplets but also their growth by condensation of the vapor phase are important.

In this paper we consider fully developed turbulent channel flow of a mixture of air and water vapor in which water droplets are dispersed. Fully developed turbulent channel flow is treated as homogeneous in the streamwise and spanwise directions [5] and therefore, periodic boundary conditions are used in these directions, as in [6].

A turbulent flow can be modeled in various ways. In this paper we make use of direct numerical simulation in which all scales of the flow, except the detailed flow around each droplet, are resolved. The solution is time dependent and the time step is limited by both stability and accuracy considerations.

In this study the mixture of air and water vapor will be referred to as the carrier phase or the carrier gas and the droplets as the dispersed phase. Incorporation of evaporation and condensation of the dispersed phase raises the question whether or not to include explicit compressibility of the carrier phase. If the carrier gas is assumed to be strictly incompressible then the inclusion of evaporation and condensation is subject to the condition that all instantaneous changes in the local mass density of air and water vapor cancel each other precisely throughout the domain. A full simulation model can be developed for such an incompressible carrier phase [7]. The incompressible treatment of the carrier phase would still permit to incorporate changes in mass density into the model using the equation of state and the Boussinesq approximation, which implies the dependence of mass density on temperature and vapor mass fraction. In our problem we relax the physical approximations further and allow the divergence of velocity not to be equal to zero as a result of phase transitions. This motivates us to treat the carrier phase as compressible flow which is characterized by a low Mach number, much smaller than 1 for the chosen initial conditions. The focus in this paper is on the development of a new low Mach number algorithm suitable for multiphase flow with phase transition, extending earlier work by Bell et al. [8]. This algorithm must be efficient for low Mach numbers: it should be possible to take a time step independent of Mach number as $Ma \rightarrow 0$.

There are two main numerical techniques for the treatment of compressible low Mach number flows: density-based methods and pressure-based methods. Two types of time-marching procedures are applied in density-based methods: explicit and implicit algorithms. Explicit density-based methods have a stability restriction, called Courant–Friedrichs–Lewy (CFL) condition [9], which makes these algorithms computationally expensive at low Mach numbers. Our previous study of turbulent droplet-laden channel flow with phase transition was done with a density-based explicit time integration method [10], which was restricted to values of the Mach number higher than the realistic value of 0.005. In implicit density-based methods the system of governing equations for compressible turbulent flow is ill-conditioned making iterative solutions excessively time consuming [11]. In order to avoid this poor condition of the numerical problem two types of schemes are used in density-based methods: preconditioning [12] and asymptotic schemes [13]. The proposed techniques are only applicable to time-independent problems. In the present study all quantities are time dependent because of the turbulent flow and the phase transitions that occur.

In order to apply preconditioning to time-dependent problems the dual-time-stepping technique is normally used [14]. The dual time-step method could also be considered for the actual compressible equations, facing the challenge of resolving very fast acoustic signals at low Mach numbers. We selected a different path and focus on the low Mach number approximation obtained as a result of asymptotic analysis and some approximations. The resulting system of equations is treated with a hybrid time stepping method. The approximated system has as virtue the absence of large eigenvalues which allows to adopt most of the terms explicitly. We closely follow the work of Bell et al. (2004) [8] and extend this to multiphase problems.

Pressure-based methods are extensions of pressure correction methods used in incompressible flow [15,16]. In incompressible flow the pressure correction follows from a Poisson equation which is obtained from the condition that the velocity field has zero divergence. In case of compressible low Mach number flow this divergence-free constraint on the velocity field is not applicable. In order to obtain a Poisson equation for the pressure an expression for the divergence of velocity is derived employing the continuity equation and the equation of state [17,8].

To obtain a suitable time integration method for the problem of droplet-laden turbulent channel flow we first perform a perturbation analysis in powers of the Mach number of the governing system of equations. An asymptotic analysis of the Navier–Stokes equations for this regime of flow conditions was conducted before in the study by Zank and Matthaeus in 1991 [18]. They derived low Mach number equations from the compressible Navier–Stokes equations employing multiple time- and space-scale expansions in powers of the Mach number. The single time-scale and multiple space-scale analysis conducted by Klein in 1995 [19] gives insight into the low Mach number Euler equations. In this paper we use a multiple time scale, single space scale low Mach asymptotic analysis closely following Müller (1998) [13] and later work of Boger et al. (2012) [20]. This approach allows to distinguish advective and acoustic modes for turbulent flows at low Mach numbers [21]. We take into account the lowest-order terms in Mach number and get a simplified system of governing equations applicable to a compressible carrier phase at low Mach numbers. The specific feature of this new system is the decomposition of pressure into two parts, one of which is independent of the spatial coordinates. This part of pressure is connected with other thermodynamic quantities through the equation of state. Another part can be called the ‘incompressible’ pressure

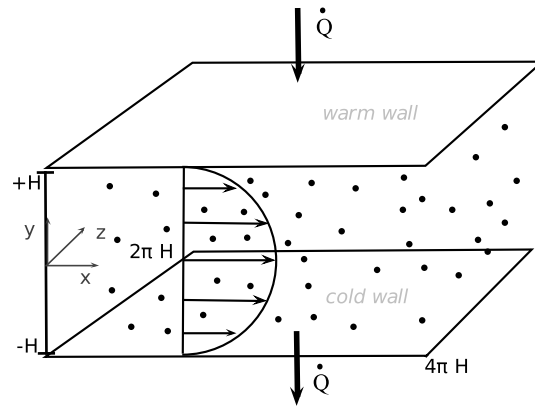


Fig. 1. The computational domain.

since it only enters the velocity equation similarly to the pressure in the incompressible formulation. The obtained splitting of pressure motivates us to use a pressure-based method. Based on the decomposed pressure, we propose a time integration algorithm extending [8] to the case of turbulent channel flow with water droplets which can undergo phase transition. This method also belongs to pressure-correction methods and we apply the continuity equation, the equation of state and the boundary conditions for the velocity in order to derive an expression for the divergence of velocity which will determine the pressure correction term.

We validate the new numerical method by comparison with results obtained with the fully explicit code in [10]. Statistical results, averaged in time and over the homogeneous directions, from both codes will be compared along with instantaneous quantities. We will quantify the accuracy of the new method first and then the gain in computing time by comparing the time it takes to simulate one time unit with the two methods.

The organization of the paper is as follows. In Section 2 we will present the mathematical model used in both codes. Next we describe in detail the low Mach number model in Section 3. In Section 4 the numerical method of the low Mach number algorithm is given. Results are presented in Section 5 and concluding remarks are collected in Section 6.

2. Governing equations for the gas–droplets system

This section is dedicated to the mathematical model which is the starting point of both the explicit numerical method and the low Mach number algorithm. First, general aspects of the problem and the geometry will be described along with the applied boundary conditions. Subsequently, the set of partial differential equations for the carrier phase, i.e., the gas consisting of air and water vapor, the system of ordinary differential equations for the dispersed phase and the source terms describing the coupling between the two phases will be presented in separate subsections.

2.1. The description of the flow domain

We consider a water–air system in a channel, bounded by two parallel horizontal plates. This is a two-phase system, consisting of a carrier phase and a dispersed phase, consisting of liquid water droplets. The carrier phase is considered using the Eulerian approach while the dispersed phase is treated in the Lagrangian manner.

In Fig. 1 a sketch of the flow domain is presented. The domain has a size of $4\pi H$ in the streamwise direction, which is denoted by x , and $2\pi H$ in the spanwise direction, z , where H is half the channel height. In addition, y is the coordinate in the wall-normal direction. The total volume of the domain is defined by V . The top wall of the channel is denoted by $y = H$ and the bottom wall by $y = -H$. Studies done by Kim et al. [6] motivate us to use periodic boundary conditions in the streamwise and spanwise directions. In addition, no-slip conditions are enforced for the carrier phase at the walls. A constant heat flux \dot{Q} is applied through the walls: this heat flux is positive through the top wall and negative through the bottom wall. The flux at both walls is equal in size in order to conserve the total energy of the system.

2.2. The governing equations

The carrier gas is treated in the Eulerian manner as a compressible Newtonian fluid. We impose conservation of mass, momentum, total energy and water vapor. The equations can be written as [3]:

$$\partial_t \rho + \partial_j (\rho u_j) = Q_m \quad (1)$$

$$\partial_t (\rho u_i) + \partial_j (\rho u_i u_j) = -\partial_j \pi_{ij} + F_i + Q_{mom,i} \quad (2)$$

$$\partial_t e_t + \partial_j (\rho u_j e_t) = -\partial_j q_j - \partial_j (u_i \pi_{ij}) + Q_e \quad (3)$$

$$\partial_t (\rho Y_v) + \partial_j (\rho u_j Y_v) = -\partial_j \phi_{v,j} + Q_m \quad (4)$$

where Q_m , $Q_{mom,i}$, Q_e are sink/source terms expressing the two-way coupling between the phases. These will be described later. In addition, (ρ, u_j, e_t, Y_v) are the carrier phase mass density, components of the velocity, total energy density and vapor mass fraction, respectively. Moreover, π_{ij} denotes pressure and viscous contributions to the momentum flux. The term F_i is an external force density which is obtained from the conservation of total streamwise momentum. In addition, q_j denotes the components of the heat flux vector, which consists of heat transport by conduction and by diffusion and the vector ϕ_v defines the diffusive mass flux of water vapor. The pressure and temperature of the carrier phase are denoted by p and T . Moreover, Y_v , p and T are connected by the ideal gas law for an air–water vapor mixture.

The dispersed phase is modeled using a point-particle approach following [3] and [4]. We solve a system of ordinary differential equations in order to find position, velocity, temperature and mass of each single droplet, $\mathbf{w}_{drop} = [\mathbf{x}_i, \mathbf{v}_i, T_i, m_i]$ of the form:

$$\frac{d\mathbf{w}_{drop}}{dt} = N_{drop} \quad (5)$$

All details of this model can be found in [10].

The interaction between the two phases is modeled by the two-way coupling terms which are derived from the conservation of the total mass, momentum, energy and water mass of the system. For instance, the two-way coupling term Q_m follows from the conservation of the total mass in the system and equals:

$$Q_m = - \sum_i \frac{dm_i}{dt} \delta(\mathbf{x} - \mathbf{x}_i) \quad (6)$$

where the sum is taken over all droplets in the domain. The expressions for the other two-way coupling terms can be found in [10].

In the next section the need for a new numerical algorithm will be clarified and the mathematical model for low Mach number flow will be derived.

3. Low Mach number model

In this section the low Mach number model will be presented. In Subsection 3.1 we will motivate the need for a new numerical algorithm. Next, in Subsection 3.2, we will describe the procedure of non-dimensionalization of the governing equations in this model. Subsection 3.3 is dedicated to the asymptotic analysis in powers of Mach number. Finally, in Subsection 3.4 we describe the solution procedure for the new system of equations.

3.1. Motivation for the new model

In order to understand better the presence of fast scales which restrict the time step in a fully explicit method, we consider the system of equations (1)–(4) in 1D for simplicity. The eigenvalues of the Jacobian matrix of this system are: $\lambda_{1,2} = u$, $\lambda_3 = u + c$ and $\lambda_4 = u - c$ where c stands for the speed of sound. If the Mach number is small, these eigenvalues define two types of time scales present in the system: the long time the flow takes to travel one length scale with the velocity u and the short time it takes for an acoustic wave to travel this length scale. Further in the text these time scales will be referred to as fast and slow scales, respectively.

In explicit numerical methods for advection–diffusion equations the restriction on the time step according to the CFL condition is given by [9]:

$$\Delta t \leq \text{CFL} \times \min \left\{ \frac{\Delta x}{|\lambda_1|}, \frac{\Delta x}{|\lambda_2|}, \frac{\Delta x}{|\lambda_3|} \right\} \quad (7)$$

where Δx is the grid spacing. We conclude that the upper bound for the time step is proportional to $\Delta x/(u \pm c)$ which is approximated by $\Delta x/c$ because we deal with a low Mach number flow. Consequently, the non-dimensional time-step is bounded by $\text{CFL} \frac{\Delta x}{c} = \text{CFL} \frac{\Delta x}{u} \frac{u}{c} = \text{CFL} \text{Ma} \frac{\Delta x}{u}$, where the grid spacing Δx and the corresponding velocity component u are non-dimensional. From a stability analysis of the Runge–Kutta method we found that in the explicit code $\text{CFL} = 2$ can be used. Consequently, the time-step which we can allow tends to zero when the Mach number tends to zero. This makes an explicit time integration computationally expensive for low Mach number flows.

It is known that for values of the Mach number up to 0.3 the fluid mechanics of single-phase turbulent channel flow corresponds well to that of incompressible flow [24,7]. However, there are three main differences between compressible and incompressible flows which can become more pronounced in case of multiphase flow with phase transitions. The characteristics of incompressible flow which are different from compressible flow are the following: a constant mass density, a zero divergence of the velocity and an infinite speed of sound. In this study compressibility appears because of changes in the mass density due to phase transitions, i.e., liquid water from the dispersed water droplets contributes to the vapor present

in the carrier phase and vice versa. This apparent compressibility is expressed by a non-zero divergence of velocity and a non-zero gradient of the mass density. If we would treat the carrier phase of the current problem as incompressible we could still incorporate changes in mass density into the model using the equation of state and the Boussinesq approximation, which implies a dependence of mass density on temperature and vapor mass fraction. However, in such an approximation the non-zero divergence of velocity is not taken into account. In [10] we quantified the explicit compressibility comparing the RMS of the term $\rho \nabla \cdot \mathbf{u}$ with the RMS of the term $\mathbf{u} \cdot \nabla \rho$ in the continuity equation. It was shown that the RMS of these two terms has the same order of magnitude. In addition, we observe a significant difference in the heat transfer characteristics of the system during the initial stages caused by a net transfer of gas when the temperature gradient develops. Therefore, we consider the carrier phase as compressible and develop a suitable numerical treatment.

3.2. Non-dimensionalization procedure

In order to eliminate stability problems related to fast time scales we replace some of the variables in the system of equations by variables which only change on the slow time scale and solve the Navier–Stokes equation partially implicitly, i.e. the pressure term is considered using implicit time-stepping. In particular, we solve the temperature equation instead of total energy density equation (3) and the vapor mass fraction equation instead of the vapor mass density equation (4):

$$\begin{aligned} & \rho (c_{pa} + Y_v(c_{pv} - c_{pa})) (\partial_t T + u_j \partial_j T) \\ & = \partial_j (K(T) \partial_j T) + \partial_j (\rho D \partial_j Y_v ((c_{pv} - c_{pa})T + \lambda_0)) + \mu(T) S_{ij} \partial_j u_i - (\lambda_0 + (c_{vv} - c_{va})T) \partial_j \rho D(T) \partial_j Y_v \\ & + Q_{temp} + \frac{Dp}{Dt} \end{aligned} \quad (8)$$

$$\partial_t Y_v + u_j \partial_j Y_v = \frac{1}{\rho} \partial_j (\rho D(T) \partial_j Y_v) + Q_{vapor} \quad (9)$$

where Q_{temp} and Q_{vapor} are two-way coupling terms which are given by:

$$Q_{vapor} = \frac{Q_m(1 - Y_v)}{\rho} \quad (10)$$

$$Q_{temp} = Q_e - u_i Q_{mom,i} - Q_m c_{vv} T + \frac{u_i^2 Q_m}{2} - Q_m \lambda_0 \quad (11)$$

The convective part of the vapor mass fraction equation is decoupled from the temperature and mass density equation (1) as can be seen in (9). Therefore, this equation only gives a diagonal term equal to u in the Jacobian matrix. The inviscid part of temperature equation (8) contains $u_j \partial_j T$ and $\frac{Dp}{Dt}$. The same reasoning as applied to the term $u_j \partial_j Y_v$ in (9) shows that $u_j \partial_j T$ does not introduce fast time scales into (8). The change of pressure, $\frac{Dp}{Dt}$, is also a slow process and does not bring fast scales into temperature equation (8). This will be clarified at the end of this section.

In order to make the system of governing equations non-dimensional we closely follow the procedure proposed by Müller (1998) [13] and choose the following reference scales: ρ_{ref} , p_{ref} , u_{ref} , T_{ref} , μ_{ref} , k_{ref} , L_{ref} , \mathcal{D}_{ref} which are the reference mass density, pressure, velocity, temperature, dynamic viscosity, thermal conductivity, length and mass diffusivity. The reference scales are chosen exactly in the way in which Müller (1998) [13] does it: this choice guarantees that non-dimensional flow quantities remain of $\mathcal{O}(1)$ for any low reference Mach number which is equal to:

$$Ma = \frac{u_{ref}}{\sqrt{\gamma p_{ref} / \rho_{ref}}} \quad (12)$$

The reference temperature and mass density are the initial mean gas temperature and mass density, respectively. The reference length is chosen as half the channel height H . The velocity scale u_{ref} is taken as the initial bulk velocity of the carrier gas u_b . All other reference scales are defined by the initial conditions which are described in Subsection 5.1. As a result of non-dimensionalization, we obtain the following system of non-dimensional equations:

$$\partial_t \rho + \partial_j (\rho u_j) = Q_m \quad (13)$$

$$\partial_t u_k + u_j \partial_j u_k + \frac{1}{\gamma Ma^2 \rho} \partial_k p = G_k + Q_{vel,k} \quad (14)$$

$$\partial_t T + u_j \partial_j T = \frac{E_T + \frac{\gamma-1}{\gamma} \frac{Dp_0}{Dt}}{\rho c_m} \quad (15)$$

$$\partial_t Y_v + u_j \partial_j Y_v = J_v + Q_{vapor} \quad (16)$$

In (14) $Q_{vel,k}$ stands for the coupling term in the velocity equation and it is equal to the following:

$$Q_{vel,k} = \frac{Q_{mom,k}}{\rho} - u_k \frac{Q_m}{\rho}. \quad (17)$$

The non-dimensional equation of state is:

$$p = \rho T (1 + MY_v) \tag{18}$$

with $M = \frac{M_{air}}{M_{water}} - 1$ where M_{air} and M_{water} are the molar masses of pure air and water, respectively. Furthermore,

$$G_k = \frac{1}{Re_b \rho} \partial_j (\mu(T) S_{kj}) + \frac{1}{\rho} F_k \tag{19}$$

where Re_b stands for the bulk Reynolds number based on the bulk velocity. Moreover, E_T in non-dimensional temperature equation (15) is a complex expression which includes the two-way coupling term Q_{temp} :

$$E_T = \frac{1}{Pr Re_b} \partial_j (\mu(T) \partial_j T) + \frac{1}{Sc Re_b} \partial_j \mu(T) \left(\partial_j Y_v ((R - 1)T + \lambda) \right) + \frac{(\gamma - 1) Ma^2}{Re_b} \mu(T) S_{ij} \partial_j u_i - \frac{1}{Sc Re_b} \left(\lambda + \left[\frac{R}{\gamma_{vapor}} - \frac{1}{\gamma} \right] T \right) \partial_j \mu(T) \partial_j Y_v + (\gamma - 1) Ma^2 Q_{temp} \tag{20}$$

where Pr , Sc denote the Prandtl number and the Schmidt number, respectively. Finally, γ_{vapor} and γ are the ratio of specific heats for water vapor and air, respectively, and $c_m = Y_v(R - 1) + 1$ with $R = \frac{c_{pv}}{c_{pa}}$. The five terms on the right-hand side of (20) correspond to the five terms on the right-hand side of dimensional temperature equation (15). The pressure derivative term is written separately for convenience of the further derivation.

In the non-dimensional vapor mass fraction equation J_v stands for:

$$J_v = \frac{1}{\rho Re_b Sc} \partial_j \mu(T) \partial_j Y_v \tag{21}$$

3.3. Asymptotic analysis

Since we only consider the low Mach number equations and ignore the fast acoustic time scale and since the governing equations only depend on the Mach number through Ma^2 , we can follow Boger et al. (2012) [20] and use an expansion of all quantities in powers of Ma^2 , e.g.:

$$p(\mathbf{x}, t, Ma) = p_0(\mathbf{x}, t) + Ma^2 p_2(\mathbf{x}, t) + Ma^4 p_4(\mathbf{x}, t) + O(Ma^6) \tag{22}$$

As a result of the choice of the reference scales, p_0, p_2, p_4 , etc., in these expansions do not depend on the Mach number [13]. We substitute all expansions in the system of governing equations (13)–(16) and (18). As a result we obtain the zeroth-order continuity equation:

$$\partial_t \rho_0 + \partial_j (\rho u_j)_0 = Q_{m,0} \tag{23}$$

Subscripts 0 in Q_m and all other expressions below indicate that the zeroth order expansion functions in the expressions of the form (22) enter these terms.

The leading momentum equations are the following:

$$\partial_j p_0 = 0 \tag{24}$$

$$\partial_t u_{k,0} + u_{k,0} \partial_j u_{k,0} + \frac{1}{\gamma \rho_0} \partial_k p_2 = G_{k,0} + Q_{vel,k,0} \tag{25}$$

The leading temperature and vapor mass fraction equations are:

$$\partial_t T_0 + u_{j,0} \partial_j T_0 = \frac{E_{T,0} + \frac{\gamma-1}{\gamma} \frac{Dp_0}{Dt}}{\rho_0 c_{m,0}} \tag{26}$$

$$\partial_t Y_{v,0} + u_{j,0} \partial_j Y_{v,0} = J_{v,0} + Q_{vapor,0} \tag{27}$$

Eqs. (23)–(27) form the final system of the governing equations together with the equation of state obtained from the asymptotic analysis:

$$p_0 = \rho_0 T_0 (1 + MY_{v,0}) \tag{28}$$

For sake of simplicity, in the following the subscript 0 will be omitted in all variables except p_0 .

3.4. Solution procedure

The solution procedure for the system of equations (23)–(28) consists of three major steps: first, finding the gas temperature and the vapor fraction at the new stage, second, finding the gas density and p_0 and third, finding the gas velocity. The first two steps are described in the text below along with the expressions for the divergence of the velocity field and the expression for $\frac{Dp_0}{Dt}$. The procedure for the velocity is an extension of the pressure-correction method and will be discussed in Section 4.1. The temperature and vapor mass fraction equations, (26) and (27), can be solved explicitly as there are no fast time scales in these equations. The coupled equations for mass density and velocity of the carrier phase, (23) and (25), still contain both small and large eigenvalues. In order to avoid the time step restriction we follow an alternative strategy which is outlined next.

A special procedure is applied to find the mass density of the carrier phase. The mass density can be calculated from equation of state (28) if apart from temperature and vapor mass fraction also p_0 would be known. In order to find p_0 we integrate (23) over the total computational domain V and obtain the total mass, m . We find an expression for the mass density from (28) and integrate it over the computational domain in order to find m using the independence of p_0 on the spatial coordinates. As a result we obtain the following expression in which m , T and Y_v are known at the new time level:

$$m = p_0 \int_V \frac{dV}{T(1 + MY_v)} \quad (29)$$

From (29) we find p_0 and subsequently the mass density is obtained from (28).

For the update of the carrier gas velocity we apply an extension of the pressure-correction procedure usually applied to incompressible flows [15]. It consists of three steps. First, a so-called ‘provisional’ velocity from the Navier–Stokes equation, based on velocity, density, temperature and pressure from the previous time is calculated. This velocity does not satisfy the correct criterion for its divergence which in case of incompressible flow is $\nabla \cdot \mathbf{u} = 0$. In order to correct the provisional velocity a Poisson equation for the pressure is solved during the second step. Finally, in the third step the provisional velocity is corrected with this pressure such that the correct divergence of velocity is obtained.

To find the divergence of velocity we start with the expression for the material derivative of p_0 following Bell et al. (2004) [8], using equation of state (28):

$$\frac{Dp_0}{Dt} = \frac{\partial p_0}{\partial \rho} \frac{D\rho}{Dt} + \frac{\partial p_0}{\partial T} \frac{DT}{Dt} + \frac{\partial p_0}{\partial Y_v} \frac{DY_v}{Dt} \quad (30)$$

Next, we substitute into the right-hand side of (30) the material derivatives $\frac{D\rho}{Dt}$, $\frac{DT}{Dt}$ and $\frac{DY_v}{Dt}$ from the governing equations (23), (26), (27). All partial derivatives on the right-hand side of (30) follow from (28). After substitution of all terms on the right-hand side of (30) we obtain:

$$\nabla \cdot \mathbf{u} = -\frac{1}{p_0} \frac{Dp_0}{Dt} + \frac{Q_m}{\rho} + \frac{1}{T\rho c_m} \left(E_T + \frac{\gamma - 1}{\gamma} \frac{Dp_0}{Dt} \right) + \frac{M}{1 + Y_v M} \left(J_v + Q_{\text{vapor}} \right) \quad (31)$$

Since $\frac{Dp_0}{Dt}$ in (31) is not known, we integrate (31) over the total computational domain. Using the boundary conditions for the velocity, i.e. no-slip boundary conditions at the walls of the channel and periodic boundary conditions in the stream- and spanwise directions, we obtain that $\int_V \nabla \cdot \mathbf{u} = 0$. Using the independence of p_0 of the spatial coordinates, we get:

$$\frac{Dp_0}{Dt} = \frac{\int_V \left[\frac{Q_m}{\rho} + \frac{E_T}{T\rho c_m} + \frac{M}{1 + MY_v} (J_v + Q_{\text{vapor}}) \right] dV}{\frac{V}{p_0} - \frac{\gamma - 1}{\gamma} \int_V \frac{dV}{T\rho c_m}} \quad (32)$$

Finally, we find the divergence of the velocity from (31). Note that expression (31) is obtained applying the specific conditions for the velocity at the boundary.

Expression (32) is also used in temperature equation (26). Since p_0 is independent of the spatial coordinates, the material derivative of p_0 is equal to $\frac{\partial p_0}{\partial t}$. We investigated the change in time of p_0 calculated from (29) and of temperature calculated with the explicit code. In the middle of the channel the relative change in temperature is 10^4 times larger than the relative change in p_0 . It means that the change of p_0 in time is a slow process and does not introduce large eigenvalues in temperature equation (26).

The forcing terms in the velocity, temperature and vapor mass fraction equations are derived from the conditions of constant momentum in all directions, constant total energy of the system and constant water vapor mass, respectively. This finishes the description of the low Mach number model. In the next section the numerical method for this model will be discussed.

4. Numerical method

The numerical method for the low Mach number model will be presented here. First, the details on the time integration algorithm will be given. Second, we will discuss the spatial discretization along with the boundary conditions and we will derive the Poisson equation for pressure and specify the method used for its solution.

4.1. Time integration algorithm

Since the term $-\frac{1}{\gamma\rho}\partial_k p_2$ in velocity equation (25) introduces large eigenvalues, we need to treat this term in an implicit way. The system of governing equations for the carrier phase (23), (25), (26) and (27) is written in the following way for the vector of unknowns $\mathbf{w} = [\rho, u_i, T, Y_v]$; the linear part consists only of the pressure term in the velocity equation:

$$\frac{\partial \mathbf{w}}{\partial t} = L(\mathbf{w}) + N(\mathbf{w}), \tag{33}$$

where L and N are linear and nonlinear operators, correspondingly, given by:

$$N(\mathbf{w}) = \begin{pmatrix} -\partial_j(\rho u_j) + Q_m \\ -u_j \partial_j u_i + \frac{1}{\rho} \partial_j(\mu(T) S_{ij}) + \frac{1}{\rho} F_i + Q_{vel,i} \\ -u_j \partial_j T + \frac{E + \frac{Dp}{Dt} + S_T}{\rho(c_{pa} + Y_v(c_{pv} - c_{pa}))} \\ -u_j \partial_j Y_v + \frac{J_v}{\rho} + Q_{vapor} \end{pmatrix}$$

and

$$L(\mathbf{w}) = \begin{pmatrix} 0 \\ -\frac{1}{\rho} \partial_i p_2 \\ 0 \\ 0 \end{pmatrix}.$$

There are not so many hybrid implicit–explicit time integration methods. We use the method proposed by Spalart et al. (1991) [25], which is a three-stage low-storage Runge–Kutta scheme of highest possible order. For the nonlinear part N each stage is analogous to forward Euler or second-order Adams–Bashforth but with different coefficients γ and ζ . For the linear part L the method is similar to the Crank–Nicolson scheme but again with different coefficients. The hybrid scheme in which the pressure term is solved implicitly is second-order accurate in time.

The solution at $t + \Delta t$, \mathbf{w}^{n+1} , is found in three substeps starting from \mathbf{w}^n at time t :

$$\mathbf{w}^{(1)} = \mathbf{w}^{(0)} + \Delta t [L(\alpha_1 \mathbf{w}^{(0)} + \beta_1 \mathbf{w}^{(1)}) + \gamma_1 N^{(0)}] \tag{34}$$

$$\mathbf{w}^{(2)} = \mathbf{w}^{(1)} + \Delta t [L(\alpha_2 \mathbf{w}^{(1)} + \beta_2 \mathbf{w}^{(2)}) + \gamma_2 N^{(1)} + \zeta_1 N^{(0)}] \tag{35}$$

$$\mathbf{w}^{(3)} = \mathbf{w}^{(2)} + \Delta t [L(\alpha_3 \mathbf{w}^{(2)} + \beta_3 \mathbf{w}^{(3)}) + \gamma_3 N^{(2)} + \zeta_2 N^{(1)}] \tag{36}$$

where $\mathbf{w}^{(n)} = \mathbf{w}^{(0)}$ and $\mathbf{w}^{(n+1)} = \mathbf{w}^{(3)}$ with the following values of the coefficients:

$$\begin{aligned} \gamma_1 &= \frac{8}{15}, & \gamma_2 &= \frac{5}{12}, & \gamma_3 &= \frac{3}{4}, & \zeta_1 &= -\frac{17}{60}, & \zeta_2 &= -\frac{5}{12}, \\ \alpha_1 &= \frac{29}{96}, & \alpha_2 &= -\frac{3}{40}, & \alpha_3 &= \frac{1}{6}, \\ \beta_1 &= \frac{37}{160}, & \beta_2 &= \frac{5}{24}, & \beta_3 &= \frac{1}{6}, \end{aligned}$$

which were obtained from the condition of highest possible order of the algorithm.

We do not solve all the quantities simultaneously. The following order is used during each stage of the time step. First, we solve the system of equations for the dispersed phase (5) explicitly using droplet and gas values at the previous stage. The right-hand sides of the droplet equations contain gas properties at the droplet location. In order to determine these, tri-linear interpolation is applied [22]. From the droplet properties at the new stage we also obtain the two-way coupling terms at this time. Next, we solve the system of equations for the carrier phase: first, we find the temperature and vapor mass fraction at the new stage, next the mass density and finally the velocity. The temperature and the vapor mass fraction equations are solved explicitly. Following the procedure for the mass density, described in the previous section, we find p_0 and the mass density by calculating the total mass in the computational domain, m , in an explicit way.

For the velocity we use an extension of the pressure-correction procedure for low Mach number compressible flows [8]. First, we find a provisional velocity \mathbf{u}^* , using the velocity, density, temperature and gradient $\partial_j p_2$ from the previous stage, i.e., this velocity is found in an explicit way. This provisional velocity does not satisfy the requirement for the divergence of velocity found in (31). During the second step we find p_2 at the new stage from the Poisson equation:

$$\nabla \cdot \left(\frac{1}{\rho^{i+1}} \nabla p_2^{i+1} \right) = \frac{\nabla \cdot \mathbf{u}^* - \nabla \cdot \mathbf{u}^{i+1}}{\beta_{i+1} \Delta t}, \tag{37}$$

where $i = 0, 1, 2$. The expression for $\nabla \cdot \mathbf{u}^{i+1}$ is known from (31). It requires $\frac{Dp_0}{Dt}$, the temperature, the vapor fraction and the mass density at the new stage. In order to find $\frac{Dp_0}{Dt}$ at the new stage the new temperature, mass density, vapor mass

fraction and p_0 are required according to (32). All these quantities were already obtained during the current stage of the time step, which makes it possible to calculate the right-hand side of Poisson equation (37) and, consequently, to solve it for the new pressure p_2^{i+1} .

During the third step of the pressure-correction procedure we apply p_2 to correct the velocity:

$$\mathbf{u}^{i+1} = \mathbf{u}^* - \Delta t \beta_{i+1} \frac{1}{\rho^{i+1}} \nabla p_2^{i+1} \quad (38)$$

In this way the new velocity \mathbf{u}^{i+1} satisfies the requirement on the divergence, (31).

4.2. Spatial discretization

The spatial discretization is based on a finite volume method which closely follows the method in [10]. The geometry is divided into rectangular cells. In the streamwise and spanwise directions a uniform grid is used, while in the wall-normal direction we apply a non-uniform grid which is finer near the walls in order to resolve the boundary layer. Throughout this paper n_x , n_z and n_y stand for the number of grid points in the streamwise, spanwise and wall-normal directions, respectively. The variables are stored in the centers of the cells. We use 128 grid points in all three directions. The choice of the grid resolution is motivated by [22] where a similar mesh was used for a finite-volume code and comparison with other methods and refinements established the degree of convergence of the solution.

The equations which we solve in the low Mach number model are not in conservative form. The treatment of the convective and viscous parts is shown for velocity equation (25). The pressure gradient is treated according to the pressure-correction procedure that was discussed above and the details on the spatial discretization of the Poisson equation will be given later in this section. The convective term in (25) $u_j \partial_j u_i$ is written as: $\partial_j u_i u_j - u_i \partial_j u_j$. The term $\partial_j u_i u_j$ is computed using a finite-volume method. For the term $u_i \partial_j u_j$ we calculate $\partial_j u_j$ with a finite-volume method and we multiply it with the value of the corresponding velocity component at the cell-center. The term $\partial_j (\mu(T) S_{ij})$ is calculated applying a finite volume method and subsequently divided by the mass density ρ in the cell center. The viscous and convective terms of Eqs. (26) and (27) are computed in a similar way.

4.3. Poisson equation

In the velocity equation (25) we do not need p_2 itself but the gradient of p_2 divided by the mass density. That is why we define a new scalar q given by:

$$\nabla q = \frac{1}{\rho} \nabla p_2 \quad (39)$$

Consequently, Poisson equation (37) can be rewritten as:

$$\Delta q = R, \quad (40)$$

where R denotes the right-hand side of the Poisson equation (37). The use of periodic boundary conditions in the homogeneous directions permits to perform a Fourier expansion of q in these directions and to apply an efficient solver for the Poisson equation. This approach is tailored to flows with two homogeneous directions and cannot easily be extended to general configurations. The Fourier coefficients \hat{q}_{k_x, k_z} depend on the wall-normal coordinate, where a pair (k_x, k_z) stands for a single Fourier mode and $0 \leq k_x \leq n_x/2$, $-n_z/2 \leq k_z \leq n_z/2$. We have a reduced number of modes in the streamwise direction because the Fourier transform of real data is such that: $\hat{q}_{-k_x, -k_z} = \hat{q}_{k_x, k_z}^*$ where \hat{q}^* denotes the complex conjugate. The Fourier expansion in the two homogeneous directions for q is:

$$q(x, y, z) = \sum_{\substack{-n_x/2 \leq k_x \leq n_x/2, \\ -n_z/2 \leq k_z \leq n_z/2}} \hat{q}_{k_x, k_z}(y) \exp^{2\pi i \left(\frac{k_x x}{L_x} + \frac{k_z z}{L_z} \right)}, \quad (41)$$

where L_x and L_z stand for the size of the computational domain in the streamwise and spanwise directions, respectively. Substituting this expansion into (40) and performing a Fourier transform of R , we obtain:

$$\left(- \left(\frac{2\pi k_x}{L_x} \right)^2 - \left(\frac{2\pi k_z}{L_z} \right)^2 + \frac{d^2}{dy^2} \right) \hat{q}_{k_x, k_z} = \hat{R}_{k_x, k_z}, \quad (42)$$

where \hat{R}_{k_x, k_z} denotes the Fourier coefficients of R . We approximate derivatives in the homogeneous directions by the derivative of the Fourier expansion.

In order to solve (42) we discretize the second derivative in the wall-normal direction of \hat{q}_{k_x, k_z} , using a five-point stencil with third-order accuracy on a non-uniform grid. On a uniform grid it becomes fourth-order accurate. As a result we obtain a linear system of equations of the form $A \hat{q}_{k_x, k_z} = \hat{R}_{k_x, k_z}$ for each pair (k_x, k_z) . The boundary conditions follow from the Navier–Stokes equation for the wall-normal velocity component, (25). Neglecting the viscous terms in this equation and

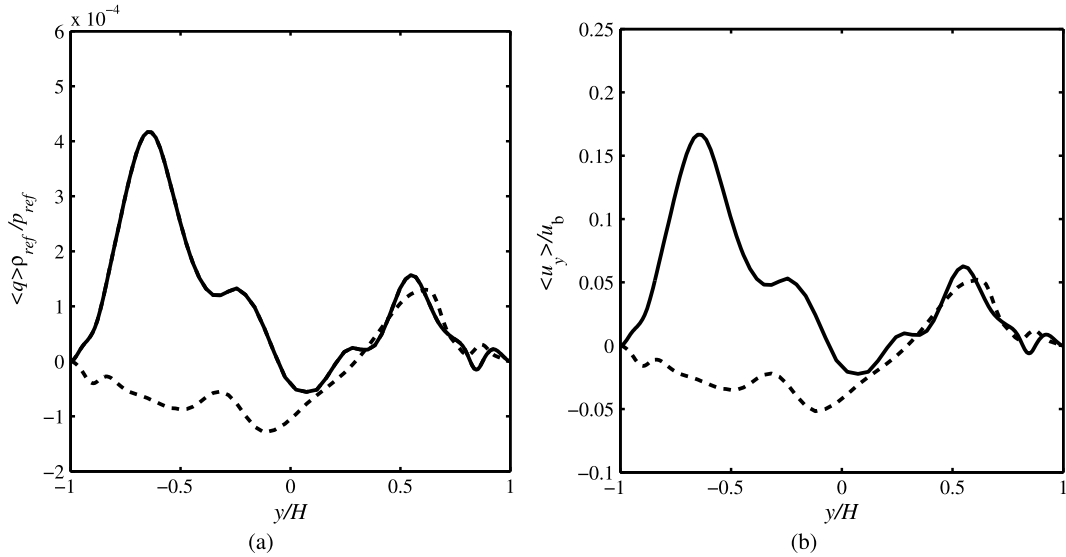


Fig. 2. (a) q , (b) wall-normal velocity component on the characteristic line perpendicular to the channel walls as a function of the wall-normal coordinate. Solid: $t = 0.1$ s, dashed: $t = 2$ s.

applying no-slip boundary conditions to the velocity, we get $\frac{1}{\rho} \frac{\partial p_2}{\partial y} \Big|_{walls} = 0$ which is equivalent to $\frac{\partial q}{\partial y} \Big|_{walls} = 0$. We discretize these boundary conditions using a three-point stencil using one ‘ghost’ cell outside the geometry at each boundary. In order to have a unique solution of the Poisson equation we need to use at least one Dirichlet boundary condition for the mode $(k_x, k_z) = (0, 0)$. At the same time the Poisson equation must satisfy the compatibility condition for a solution to exist:

$$\int_{-H}^H \hat{R}_{k_x, k_z} dy = 0 \tag{43}$$

We use the Dirichlet condition at one wall and the Neumann boundary condition at the other. The Neumann condition at the first wall will be satisfied, since the compatibility condition is satisfied.

Solving $A \hat{q}_{k_x, k_z} = \hat{R}_{k_x, k_z}$ for each Fourier mode (k_x, k_z) using LU-decomposition of matrix A , we find \hat{q} and, consequently, perform a back Fourier transform to find q . As was stated above, we do not need the pressure p_2 itself but in principle it can be computed from (39) by integration since ρ and q are both known.

In this study we use a collocated grid with variables stored in cell centers. The fluxes at the cell faces are found using linear interpolation of the corresponding quantities. This approach is known to lead to odd–even decoupling in some cases, resulting in oscillations in pressure and velocity fields. The solution for q and the wall-normal velocity component were found not to suffer from this effect with the current method, as is illustrated in Fig. 2(a) and Fig. 2(b), which display smooth dependency of typical solution components on the spatial coordinates.

4.4. Boundary conditions

We apply periodic boundary conditions in the streamwise and spanwise directions for all variables. For the vapor mass fraction we use $\frac{\partial Y_v}{\partial y} \Big|_{walls} = 0$ in order to avoid diffusion of vapor through the walls. The boundary condition at the walls for the temperature of the carrier gas is found from the condition of constant heat flux to the walls, q_{wall} :

$$q_{wall} = -k(T) \frac{\partial T}{\partial y} \Big|_{walls} \tag{44}$$

Keeping q_{wall} constant we can find the wall-normal derivative of the temperature at the walls, using one ‘ghost’ point outside the geometry at each wall.

For the droplets periodic conditions are used in the homogeneous directions. This means that if a droplet leaves the domain, it re-enters the domain from the other side with the same properties. Moreover, droplets collide elastically with the walls if they approach the wall within a distance of their radius.

5. Validation of the method

This section consists of two parts: specification of the initial conditions for the simulations and presentation of the results. In the results part we will compare the results and efficiency of the low Mach number code with the explicit code,

Table 1
Non-dimensional parameters of the simulation.

Re_b	Pr	Ma	Sc
2333	0.7478	0.05	0.06283

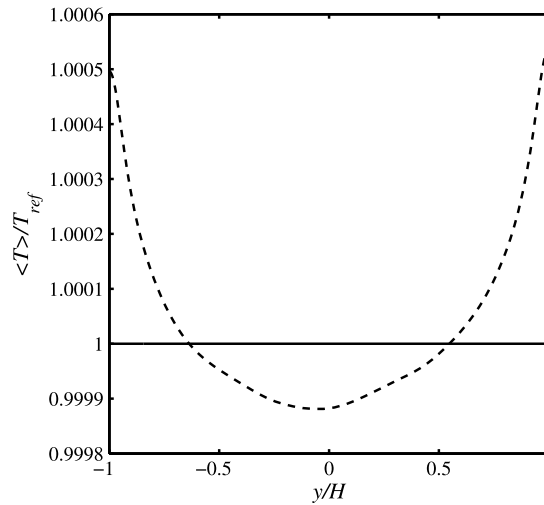


Fig. 3. Initial gas temperature averaged over the homogeneous directions as a function of the wall-normal coordinate. Solid: low Mach number code, dashed: explicit code.

thereby establishing the accuracy of the expansion in the Mach number including zeroth order for all solution components apart from the pressure for which also the second-order term in the expansion is retained.

5.1. Initial conditions

In both codes the simulations are started from a turbulent velocity field, obtained from a simulation without droplets at the correct value of the Mach number with adiabatic boundary conditions. This simulation was done with the fully explicit code until the statistically steady state was reached in which the solution fluctuates around a well-defined mean state.

The developed numerical method can be applied to any initial conditions but since the results from the fully explicit code are available we use the following initial condition: atmospheric pressure, room temperature and relative humidity equal to 100% which corresponds to one of the simulated cases in [10]. The values of the thermodynamic parameters of the flow can be found in [10] for a mean temperature of 293.15 K. The initial conditions determine the non-dimensional parameters of the simulation are shown in Table 1.

The Mach number, $Ma = 0.05$, does not correspond to the reference velocity; the actual Mach number is ten times smaller. The motivation for the adopted value is CFL condition (7): at this Mach number the explicit code can be applied with an acceptable amount of computing time, thus providing a point of reference for the current new algorithm [10]. In [10] it was shown that for this Mach number the flow physics and heat and mass transfer characteristics are accurately approximated comparing results of the compressible formulation with those of an incompressible model.

In all results shown in this paper the initial conditions are chosen in the following way. For the explicit solver a snapshot of the solution in the statistically steady state was chosen of the same system of equations, but in the absence of droplets and with adiabatic boundary conditions. For the low Mach number solver the same initial velocity field was used, but the temperature and mass density were taken constant, corresponding to the solution of the system of equations (23)–(28) in the statistically steady state for adiabatic boundary conditions. The differences in the initial temperature between the two solvers are of order Ma^2 and can be seen in Fig. 3. The initial vapor mass fraction is for both solvers found from the condition of 100% relative humidity.

This particular method for choosing the initial conditions for the low Mach number solver depends on the availability of an explicit solver. In order to avoid this restriction, we verified that the low Mach number solver can also be used to simulate the same flow starting from a laminar velocity profile onto which small two- and three-dimensional perturbations were superposed. Indeed, we found that the differences in statistical properties of the solutions arising from these two initial conditions are negligible.

We randomly distribute 2 000 000 droplets over the volume of the channel. The initial droplet diameter is given by $d_i/H = 3.09 \times 10^{-3}$. The initial droplet diameter satisfies the conditions for the point-particle approach [10]. The initial volume fraction of droplets is on the order of 10^{-4} . According to the classification in [23] this fraction is high enough so

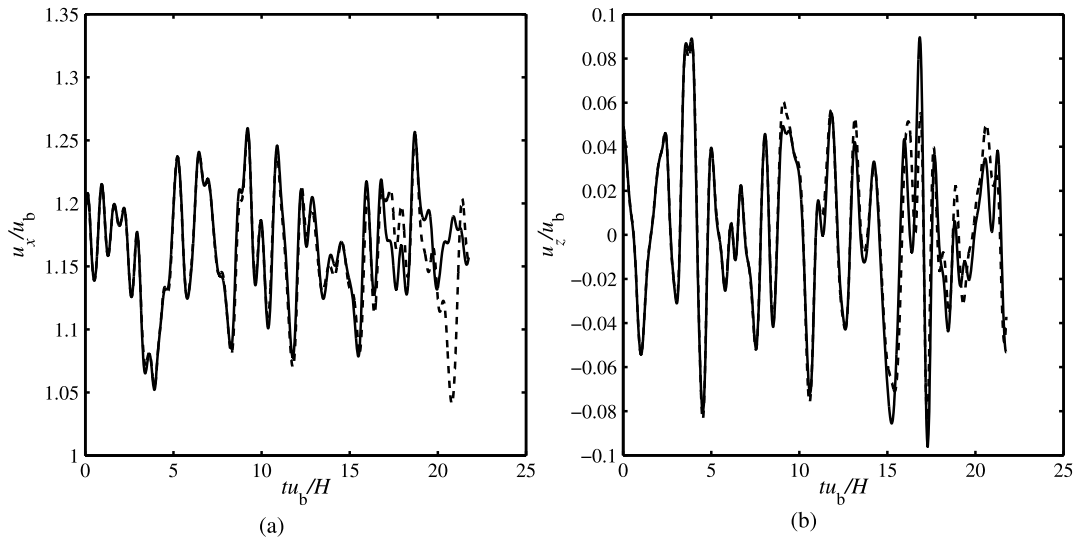


Fig. 4. (a) Streamwise velocity component, (b) spanwise velocity component at point $(0.3H, 0.15H, 0)$ as a function of time. Solid: low Mach number code, dashed: explicit code.

that two-way coupling is required and low enough for the effects of collisions between droplets to be negligible. Velocity and temperature of the droplets are initialized using the carrier gas values at the droplet locations.

5.2. Comparison of results from the two codes

Comparison of the results from the two algorithms, i.e., the explicit method and the hybrid approach, can be performed in two ways. For short times local, instantaneous results can be compared. For turbulent flow, however, small differences in initial conditions or in algorithms lead to large differences after a finite time. Therefore, instantaneous results cannot be compared over longer time intervals. In the turbulent regime with time-independent boundary conditions, the flow reaches a statistically steady state in which the solution fluctuates around a mean. The statistically steady state can be compared for both methods. The second method of validation is therefore based on a comparison of statistical quantities in this statistically steady state. Statistical results are obtained by averaging over the homogeneous directions and over time. Since the error in statistical quantities depends on the time interval used for averaging we cannot expect smaller differences between the statistical results from the two solvers than this time-averaging error, which is estimated around 1% for the current simulation and averaging time [26]. Throughout the paper quantities averaged over the homogeneous directions and over time will be denoted by brackets, $\langle \cdot \rangle$. Averaging over the homogeneous directions at a certain time is denoted by bars, $\bar{\cdot}$. All results are presented in non-dimensional units.

5.2.1. Instantaneous results

First, the time history of the streamwise and spanwise components of the gas velocity are compared in one point in the middle of the channel. Figs. 4(a) and 4(b) show a close agreement in the velocity components even up to time 15, corresponding to $15H/u_b$ flow-through times. Until this moment, the difference is on the order of 1%.

In the sequel differences in the results on the order of 1% will be referred to as close or good agreement. This order of difference is considered to be acceptable to conclude that the developed low Mach number model can be used for simulating turbulent droplet-laden channel flow with phase transitions.

5.2.2. Mean results

The carrier gas reaches a statistically steady state for which the mean profiles are determined after time $150H/u_b$. In Fig. 5 the instantaneous temperature near the bottom wall is shown. We observe that after time $150H/u_b$ changes in the gas temperature are less than 1% with respect to the reference temperature; that condition was selected to start averaging from this time. The time averaging for all quantities is performed over the interval $[150H/u_b; 700H/u_b]$. Based on the statistical errors calculated in [26] for a similar system we estimate that averaging over the chosen interval results in maximum statistical relative errors on the order of less than 1% in all quantities and to errors on the order of 1% in their RMS.

Fig. 6 shows a good agreement between the low-Mach model and the fully compressible model in the mean temperature of the carrier phase and in the rms of the wall-normal component of the velocity. To quantify this agreement we calculate the relative difference which is equal to the L^2 -norm of the difference between the results of the two codes, divided by the L^2 -norm of the result of the low Mach number code:

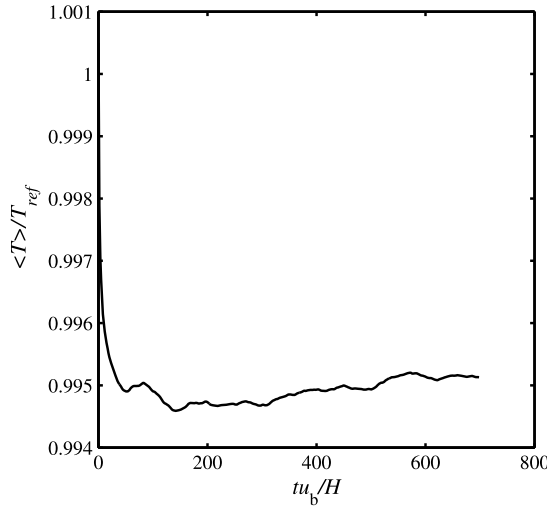


Fig. 5. Gas temperature at point $(0.3H, 0.15H, -0.012H)$ history in the low Mach number code.

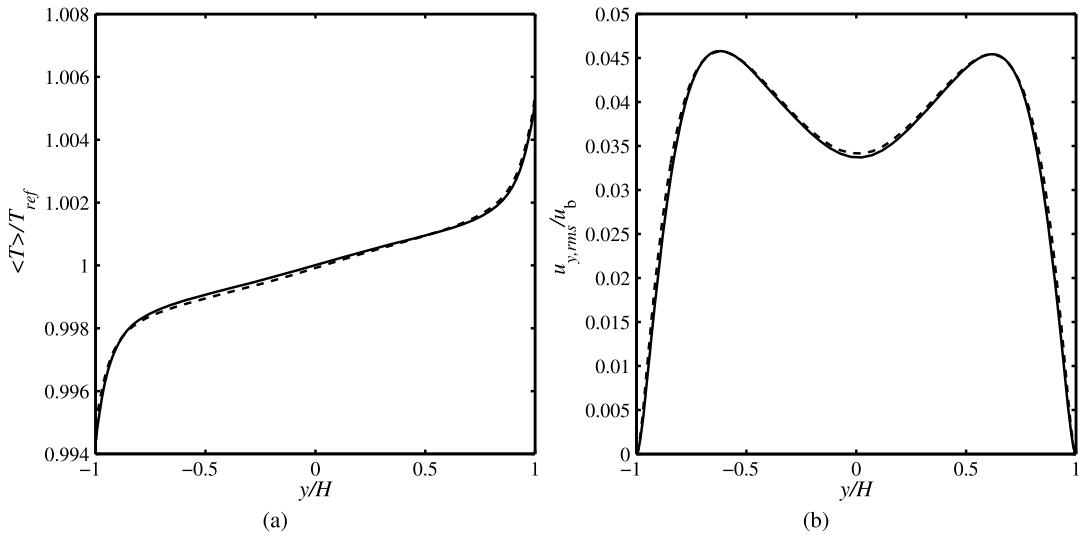


Fig. 6. (a) Mean gas temperature and (b) RMS of the wall-normal gas velocity as a function of the wall-normal coordinate. Solid: low Mach number code, dashed: explicit code.

$$\Delta = \frac{\sqrt{\sum_{k=1}^{n_y} (\langle u \rangle_k^{Mach} - \langle u \rangle_k^{expl})^2}}{\sqrt{\sum_{k=1}^{n_y} (\langle u \rangle_k^{Mach})^2}} \tag{45}$$

where the superscripts *Mach* and *expl* denote the low Mach number code and the explicit code, respectively. The relative difference Δ is below 3% for the rms of the wall-normal velocity for the time interval considered. Quantifying the difference between the results of the two codes in the gas mean temperature, it makes sense to divide it by the difference in the mean gas temperature between the two walls in the low Mach number code which is the quantity of interest for this problem. Calculating in this way, Δ is equal to 1% for the mean gas temperature.

We consider the Nusselt number to express the efficiency of the heat transfer between the channel walls. The Nusselt number is defined in the following way:

$$Nu = \left(\frac{d\bar{T}_g}{dy} \Big|_{wall} \right) / \frac{\Delta \bar{T}_g}{2H} \tag{46}$$

where ΔT_g is the difference in gas temperature between the two walls and the derivative with respect to the wall-normal coordinate in the numerator is the average over both walls. We compare the history of the Nusselt number in Fig. 7, which shows a close agreement. The relative difference in the Nusselt number averaged in time over the steady state is equal to

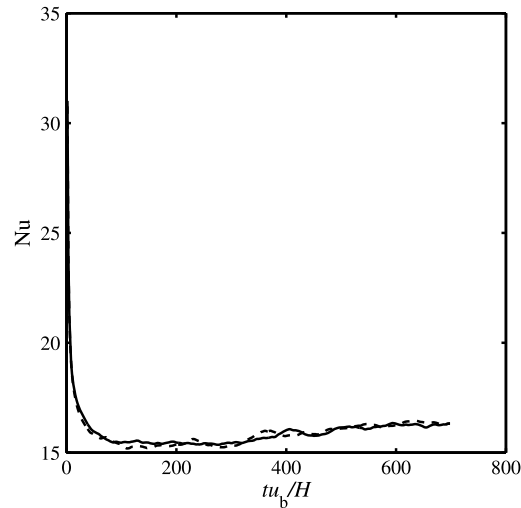


Fig. 7. Nusselt number history. Solid: low Mach number code, dashed: explicit code.

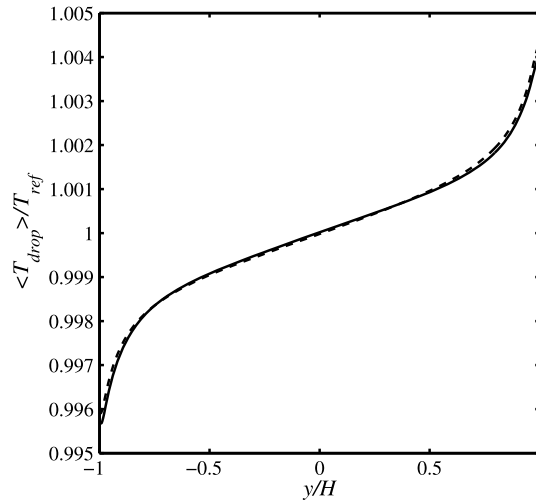


Fig. 8. Droplet mean temperature as function of the wall-normal coordinate. Solid: low Mach number code, dashed: explicit code.

0.1%. The droplet mean temperature in Fig. 8 shows a good agreement between the two codes with a relative difference Δ equal to 3%. This difference is made non-dimensional using the difference in the mean droplet temperature between the two walls, found with the low Mach number method.

We also consider the droplet size probability density function (PDF) near the walls, Figs. 9(a) and 9(b). In order to compute this PDF, the wall-normal direction was divided into 64 equidistant slabs parallel to the channel walls. In each slab we distinguish 100 bins representing different diameter ranges distributed uniformly between d_{min} and d_{max} which are the minimum and maximum diameter among the droplets present in a certain slab. Next we compute for each slab the number of droplets within a certain bin. The size is normalized with the initial droplet diameter, d_0 . The figure shows a good agreement between the results of the two codes for this quantity. In order to verify that the differences between the two codes are on the order of Ma^2 we also performed the simulation with the two codes for $Ma = 0.1$, Fig. 9(c). In order to quantify the difference in the droplet size PDF in the two formulations we compute the L^2 -norm of the difference. We find that the norm of the differences between the results for $Ma = 0.1$ is four times larger than this norm for $Ma = 0.05$. This illustrates that the difference between the two methods is on the order of Ma^2 . The same result for the difference between the results of the two codes was found for the gas and droplet temperature averaged in time and in the homogeneous directions.

The comparison of the results of the two methods shows a good agreement: the differences in the kinematic and heat transfer properties along with the droplet characteristics are on the order of 1%. Next we will quantify the extent by which the new low Mach number method permits to simulate more efficiently than the explicit method at low Mach numbers.

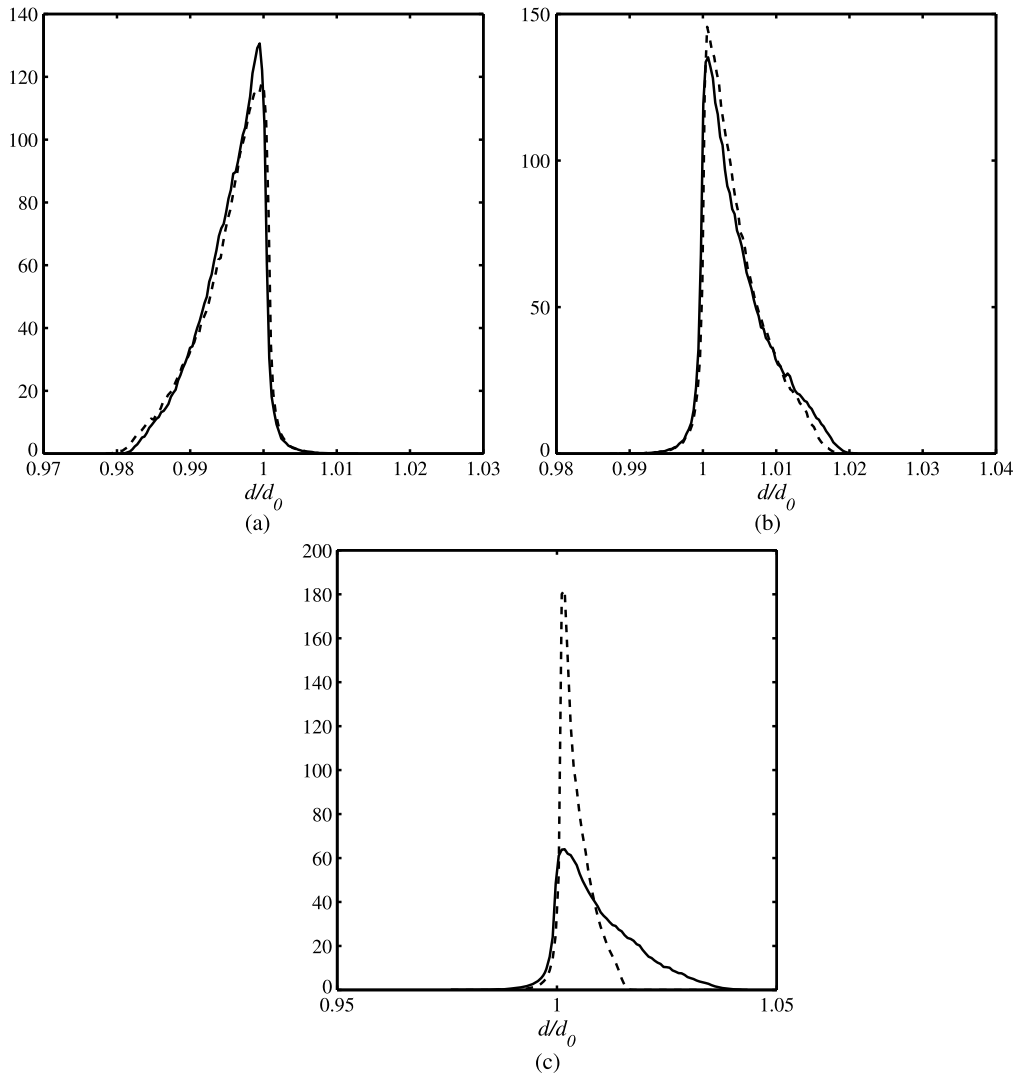


Fig. 9. Droplet size PDF at time 300: (a) near the hot wall, (b) near the cold wall. (c) Droplet size PDF at time 300 near the cold wall for $Ma = 0.1$. Solid: low Mach number code, dashed: explicit code.

5.2.3. Stability analysis and the time step

We performed a stability analysis for both the explicit method (1)–(4) and the low Mach number algorithm (23)–(28) in the same way as done by Müller and Rizzi [27] for an explicit algorithm for compressible, viscous flow. The stability analysis consists of two parts. First, the equations are linearized and discretized in space. This leads to a large system of coupled, linear ordinary differential equations. Fourier analysis results in a diagonal system of equations of the form:

$$\frac{d\mathbf{v}}{dt} = \Lambda \mathbf{v} \quad (47)$$

where \mathbf{v} represents the vector of amplitudes of the Fourier modes and Λ is a diagonal matrix which contains the complex eigenvalues, λ_i . Second, the regions in which $\lambda_i \Delta t$ is stable for the specific Runge–Kutta schemes used in this paper are determined.

Following [27] for our systems of equations, we find that the diffusive terms in the equations lead to:

$$\frac{-4}{Re_b Sc \Delta x^2} < \text{Re}(\lambda_i) < 0 \quad (48)$$

for both methods. For the explicit algorithm the convective terms lead to:

$$|\text{Im}(\lambda_i)| < \frac{u}{Ma \Delta x} \quad (49)$$

and for the low Mach number algorithm:

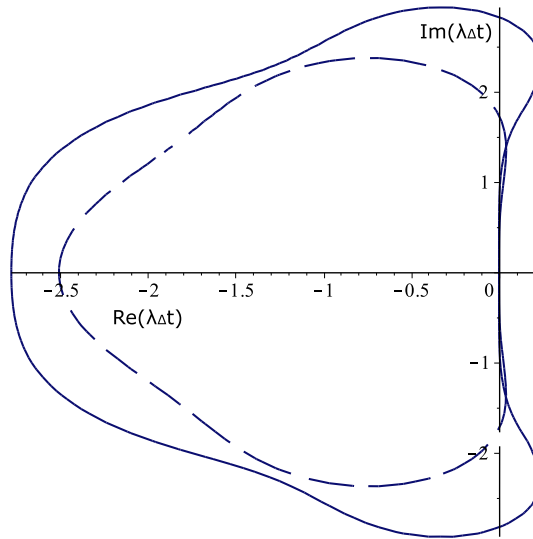


Fig. 10. The outer bound of the stability region for solid: RK3 dashed: RK4. The figure shows the region in which the amplification factor of the scheme is smaller than 1.

$$|\text{Im}(\lambda_i)| < \frac{u}{\Delta x} \tag{50}$$

where u is a typical value for the velocity and Δx the typical grid size.

Fig. 10 shows the regions in which $\lambda_i \Delta t$ should be to obtain stability for both algorithms. It turns out that for the parameters used in our simulations the diffusive terms lead to the most severe restriction on the time step for the low Mach number algorithm, whereas the convective terms are most restrictive for the explicit method. The explicit method is stable if $\Delta t < \text{RK} \frac{\Delta x^2 \text{Re} \text{Sc}}{4}$ with $\text{RK} = 2$ and $\Delta t \leq \text{CFL} \times \text{Ma} \frac{\Delta x}{u}$ with $\text{CFL} = 2$. For the low Mach number code the time step should satisfy $\Delta t < \text{RK} \frac{\Delta x^2 \text{Re} \text{Sc}}{4}$ with $\text{RK} = 2$ and $\Delta t < \text{CFL} \times \text{Ma} \frac{\Delta x}{u}$ with $\text{CFL} = 1$. Substituting the non-dimensional parameters of the simulation $\text{Re}_b = 2333$, $\text{Sc} = 0.632799$ and $\Delta x = 0.004$, we obtain as time step limits 0.01 in the low Mach number code and 0.0004 in the explicit code.

We notice from the above restrictions on the time step in the low Mach number solver that the relevant bounds do not depend on the Mach number. As a result, we can simulate flows at different small Mach numbers with the same time step. This big advantage of the low Mach number method can also be shown analytically. As a result of making the system of governing equations for the carrier gas non-dimensional the Mach number is present in the temperature equation (26) only. In fact, the third and fifth terms on the right-hand side of (26) depend explicitly on the Mach number. It follows that the sum of the Mach number dependent terms in (26) is of order 1 with corrections which are of second order in the Mach number. Consequently, if the Mach number goes to zero, the dependence of the temperature equation on Mach number vanishes and, consequently, the system of governing equations does not depend on the Mach number. As a result, we can simulate flows at different small Mach numbers with the same time step. This was separately verified by performing simulations for three different small values of the Mach number, $\text{Ma}_1 = 0.005$, $\text{Ma}_2 = 0.025$ and $\text{Ma}_3 = 0.05$, using the maximum possible time step in the low Mach number code of 0.01. Knowing that the changes in the gas temperature are of order Ma^2 , $T(\text{Ma}) = T(0) + \alpha \text{Ma}^2 + \dots$, with constant α we expect:

$$R_{\text{Ma}} = \frac{T(\text{Ma}_3) - T(\text{Ma}_1)}{T(\text{Ma}_2) - T(\text{Ma}_1)} = 4.125 \tag{51}$$

Fig. 11 shows that the difference $4.125 \times (T(\text{Ma}_2) - T(\text{Ma}_1))$ and $T(\text{Ma}_3) - T(\text{Ma}_1)$ is in close agreement at the arbitrary chosen point $(0.3H, 0.15H, -0.012H)$. We also plotted the difference $(T(\text{Ma}_3) - T(\text{Ma}_1)) - (T(\text{Ma}_2) - T(\text{Ma}_1)) \times 4.125$ which has a magnitude of 10^{-8} .

5.3. Computational efficiency

In the previous subsection the optimal time steps for the two solvers were determined. For the chosen grid and $\text{Ma} = 0.05$ the time step in the explicit solver has to be approximately 25 times smaller than the time step in the low Mach number solver.

We found that one time step with either method requires approximately the same CPU time on the same computer. A realistic Mach number, which in our test case is equal to 0.005, would require a further reduction in the time step by a factor of ten in the explicit code. In the low Mach number code there is no need to decrease the time step because of its independence on the Mach number, as discussed in the previous subsection. Consequently, we may conclude that the

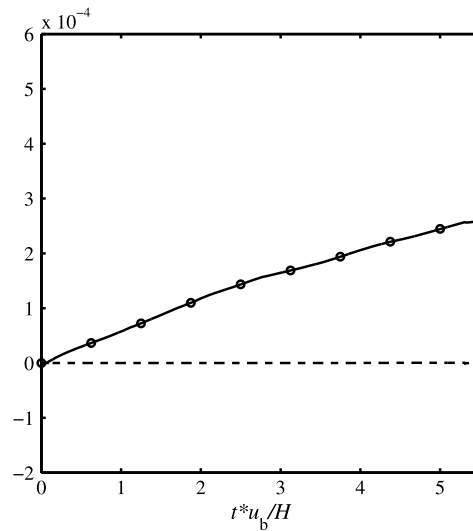


Fig. 11. Solid: $4.125 \times (T(\text{Ma}_2) - T(\text{Ma}_1))$ at point $(0.3H, 0.15H, -0.012H)$, circles: $T(\text{Ma}_3) - T(\text{Ma}_1)$ at point $(0.3H; 0.15H; -0.012H)$, dashed: difference between these two curves at the same point as functions of time.

problem considered here can be simulated approximately 250 times faster with the new numerical method than with the fully explicit code for the realistic small value of the Mach number.

Finally, we verified that using a 25 times larger time step in the low Mach number solver, compared to the explicit method at $\text{Ma} = 0.05$, yields deviations less than 1% in mean quantities such as gas velocity and temperature. This shows that the larger time step for the low Mach number solver is adequate for obtaining accurate results even though the asymptotic low Mach number analysis is adopted at this relatively high Mach number.

6. Conclusions

In this paper a new numerical approach for simulating droplet-laden turbulent channel flow with phase transitions at low Mach numbers was proposed. It is based on an asymptotic analysis at low Mach numbers. This numerical approach is beneficial because it avoids the dependence of the time step on Mach number arising from a CFL constraint on the time step in explicit time integration methods for low Mach numbers.

Results from the new low Mach number code were compared with results of a fully explicit code. We observe a good agreement in local instantaneous quantities along with a good agreement in mean quantities for both phases. The relative difference is equal to 1% in the mean gas temperature and 3% in the droplet mean temperature. Moreover, we observe a close agreement between the results of the two codes in the droplet size PDF at a single time along with a good agreement in the Nusselt number history. This establishes the overall accuracy of the new low Mach number formulation.

It was shown that the time step in the low Mach number code can be chosen independently of Mach number. This was observed from numerical experiments at different low Mach numbers, which confirms the analysis of the dependence of the governing equations on Mach number. As a result, the flow at the realistic Mach number of $\text{Ma} = 0.005$ for the current flow conditions can be simulated approximately 250 times faster with the new solver. This gain in time will be used in future work to examine different initial conditions which give rise to processes where compressibility effects become more important.

Acknowledgements

This work is supported through a PhD grant within the FOM 08DROPO2-2 program. This work was sponsored by the Stichting Nationale Computerfaciliteiten (National Computing Facilities Foundation, NCF) for the use of supercomputer facilities, with financial support from the Nederlandse Organisatie voor Wetenschappelijk Onderzoek, NWO (project SH-061).

References

- [1] M. Barigou, S. Mankad, P.J. Fryer, Heat transfer in two-phase solid–liquid food flows, *Trans. Inst. Chem. Eng.* 76 (1998) 3–29.
- [2] F. Mashayek, Droplet–turbulence interactions in low-Mach-number homogeneous shear two-phase flows, *J. Fluid Mech.* 367 (1998) 163–203.
- [3] R.S. Miller, J. Bellan, Direct numerical simulation of a confined three-dimensional gas mixing layer with one evaporating hydrocarbon-droplet-laden stream, *J. Fluid Mech.* 384 (1998) 293–338.
- [4] E. Masi, O. Simonin, B. Bédard, The mesoscopic Eulerian approach for evaporating droplets interacting with turbulent flows, *Flow Turbul. Combust.* 86 (2010) 563–583.
- [5] St.B. Pope, *Turbulent Flows*, Cambridge University Press, 2000.

- [6] J. Kim, P. Moin, R. Moser, Turbulence statistics in fully developed channel flow at low Reynolds number, *J. Fluid Mech.* 177 (1987) 133–166.
- [7] E. Russo, J.G.M. Kuerten, C.W.M. van der Geld, B.J. Geurts, Water droplet condensation and evaporation in turbulent channel flow, *J. Fluid Mech.* 749 (2014) 666–700.
- [8] J.B. Bell, M.S. Day, C.A. Rendleman, S.E. Woosley, M.A. Zingale, Adaptive low Mach number simulations of nuclear flame microphysics, *J. Comput. Phys.* 195 (2004) 677–694.
- [9] K.W. Morton, D. Mayers, *Numerical Solution of Partial Differential Equations*, second ed., Cambridge University Press, 2005.
- [10] A. Bukhvostova, E. Russo, J.G.M. Kuerten, B.J. Geurts, Comparison of DNS of compressible and incompressible turbulent droplet-laden heated channel flow with phase transition, *Int. J. Multiph. Flow* 63 (2014) 68–81.
- [11] S. Røller, C.D. Munz, A low Mach number scheme based on multi-scale asymptotics, *Comput. Vis. Sci.* 3 (1/2) (2000) 85–91.
- [12] E. Turkel, Preconditioned methods for solving the incompressible and low speed compressible equations, *J. Comput. Phys.* 72 (1987) 277–298.
- [13] B. Müller, Low-Mach-number asymptotics of the Navier–Stokes equations, *J. Eng. Math.* 34 (1998) 97–109.
- [14] B. Lessani, Large-eddy simulation of turbulent flows. Application to low Mach number and particle-laden flows, PhD thesis, Vrije Universiteit Brussel, 2003.
- [15] C.A.J. Fletcher, *Computational Techniques for Fluid Dynamics*, Springer-Verlag, Berlin, Heidelberg, 1988.
- [16] K. Karki, S.V. Patankar, Pressure based calculation procedure for viscous flows at all speeds in arbitrary configurations, *AIAA J.* 27 (9) (1989) 1167–1174.
- [17] A.W. Vreman, R.J.M. Bastiaans, B.J. Geurts, A similarity subgrid model for premixed turbulent combustion, *Flow Turbul. Combust.* 82 (2009) 233–248.
- [18] G.P. Zank, W.H. Matthaeus, The equations of nearly incompressible fluids I. Hydrodynamics, turbulence, and waves, *Phys. Fluids A* 3 (1991) 69–82.
- [19] R. Klein, Semi-implicit extension of a Godunov-type scheme based on low-Mach-number asymptotics, I: One-dimensional flow, *J. Comput. Phys.* 121 (1995) 213–237.
- [20] M. Boger, F. Jaegle, R. Klein, C.-D. Munz, A pressure-based numerical method for the simulation of compressible two-phase flow, in: *Proceedings of 12th Triennial International Conference on Liquid Atomization and Spray Systems*, Heidelberg, Germany, September 2012.
- [21] J.R. Ristorcelli, A closure for the compressibility of the source terms in Lighthill's acoustic analogy, *ICASE Report No. 97-44*, 1997, 20 pp.
- [22] C. Marchioli, A. Soldati, J.G.M. Kuerten, B. Arcen, A. Tanière, G. Goldensohn, K.D. Squires, M.F. Carnelutti, L.M. Portela, Statistics of particle dispersion in direct numerical simulations of wall-bounded turbulence: results of an international collaborative benchmark test, *Int. J. Multiph. Flow* 34 (9) (2008) 879–893.
- [23] S. Elghobashi, On predicting particle-laden turbulent flows, *Appl. Sci. Res.* 52 (1994) 309–329.
- [24] J.D. Anderson, *Fundamentals of Aerodynamics*, fifth ed., McGraw-Hill Ser., 2007.
- [25] P.R. Spalart, R.D. Moser, M.M. Rogers, Spectral methods for the Navier–Stokes equations with one infinite and two periodic directions, *J. Comput. Phys.* 96 (1991) 297–324.
- [26] A.W. Vreman, J.G.M. Kuerten, Comparison of direct numerical simulation databases of turbulent channel flow at $Re_\tau = 180$, *Phys. Fluids* 26 (2014) 015102.
- [27] B. Müller, A. Rizzi, Navier–Stokes computation of transonic vortices over a round leading edge delta wing, *AIAA-87-1227*, 1987.